ELSEVIER

Powder Technology 119 (2001) 134–152

POWDER TECHNOLOGY

www.elsevier.com/locate/powtec

Mixing and dispersion of particle ropes in lean phase pneumatic conveying

Harun Bilirgen, Edward K. Levy *

Energy Research Center, Lehigh University, 117 ATLSS Drive, Bethlehem, PA 18015, USA

Received 21 August 2000; received in revised form 4 November 2000

Abstract

The objective of this study was to investigate mixing mechanisms in lean phase pneumatic conveying, with the emphasis on techniques for dispersing the severe particle stratification caused by flow through a 90° elbow. This type of stratification is referred to as a particle rope. The paper describes a combined numerical and experimental study of the rope dispersion characteristics of various mixing devices that were installed immediately downstream of the elbow. The laboratory experiments were conducted in a 0.154 m I.D. vertical test section. Local particle velocities and concentrations were measured using a reflective type fiber optic probe. The numerical simulations were carried out using the CFX-4.2 code developed by AEA Technology.

The effect of secondary velocities on rope dispersion was investigated by using a flow straightener installed after the elbow. The results show that the rope dispersion rate in both the axial and radial directions was significantly reduced in the absence of secondary velocities.

The types of flow mixers investigated included nozzles, air jet injection, and swirl vanes. Although all mixing techniques were able to disperse the particle rope within nine pipe diameters from the bend exit plane, nozzles with beta ratios of 0.5 and 0.67 and air jet injection from the inner wall caused the most rapid rope dispersion. However, the nozzles cause excessive pressure drop and the air jet injection technique increases the flow rate of conveying fluid carried by the pipe.

Keywords: Mixing; Dispersion; Particle ropes; Lean phase pneumatic conveying

1. Introduction

Pipe bends are a common feature of most pneumatic conveying systems and are well known to create flow problems, even in single phase flows. The situation is further complicated with the presence of a solid phase, such as occurs in pneumatic conveying. As the air–particle mixture approaches the pipe bend, a double vortex flow structure occurs in the fluid phase and a significant phase separation in the particulate phase is experienced within the bend geometry due to centrifugal forces. Upon exiting from the bend, the particles flow together in a narrow localized stream (see Fig. 1) and the velocity of the particles in the suspension is reduced to almost one half of the mean gas velocity. This phenomenon is referred to as "roping". Once formed, this flow stratification pattern can persist over a region extending up to 25 pipe diameters downstream of the elbow. It eventually breaks down due to flow turbulence and to the secondary flow induced by the elbow.

The objective of the present study was to identify ways to quickly dissipate a rope-like structure and achieve a homogeneous distribution of the two phase mixture over the pipe cross-section within short distances from the bend exit. Since naturally occurring mechanisms such as flow turbulence and secondary flow patterns with a plain elbow are not sufficient to achieve this, the use of mechanical mixing devices is necessary for promoting rapid mixing of the flow. A detailed investigation, including laboratory experiments and numerical simulations, was carried out to understand the rope mixing processes with different types of devices.

The present study focuses on dilute phase pneumatic conveying. The air-to-solids mass loading ratios were typi-

* Corresponding author. Tel.: +1-610-758-4090; fax: +1-610-758-5959.

E-mail address: ekl0@lehigh.edu (E.K. Levy).

0032-5910/01/$ - see front matter
PII: S0032-5910(00)00413-7

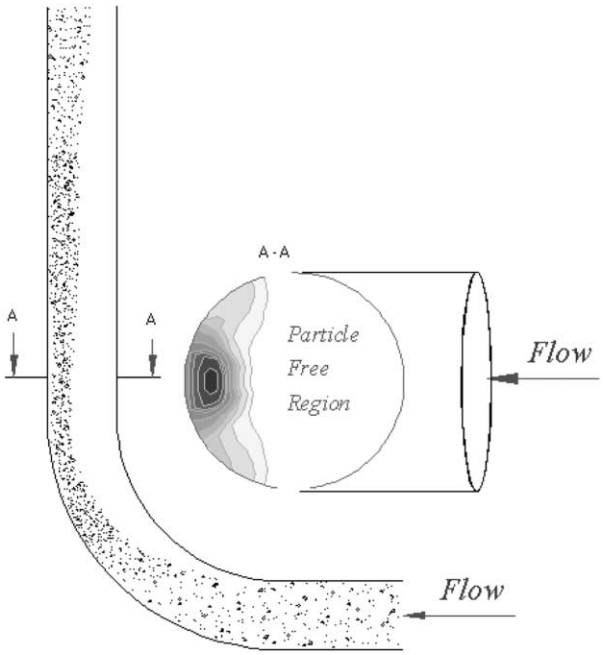

Fig. 1. Particle roping.

cally in the range of 1–3 and the average air velocity was between 15 and 30 m/s.

2. Experimental apparatus

Fig. 2 shows the experimental test facility used for this study. Air is supplied by compressors that provide a maximum air velocity of 30 m/s in the 0.154 m I.D. test section. Particles stored in hopper (1) are discharged into the inlet air stream at (6) via a screw feeder. The flow mixing mechanisms were positioned immediately after the elbow (7). Instrument ports allow measurements of particle flow patterns in the vertical test section downstream of the pipe bend. At the end of the upper horizontal pipe, the particles are separated from the air using a cyclone separator (3), and any remaining fine particles are removed in the fabric filter (4).

Table 1
Particle size distribution of conveyed material (coal)

Diameter (μm)	Weight (%)
> 125	0.05
106–125	0.27
90–106	1.73
75–90	15.46
63–75	14.54
45–63	22.50
< 45	45.44

The experiments were performed with coal particles with a mean diameter of 59 μm and a density of 1680 kg/m^3. The particle size distribution is given in Table 1.

Local particle concentration and velocity measurements were performed using a reflective type fiber optic probe that was traversed over the cross-section of the pipe to obtain detailed profiles. Information about the probe is given by Refs. [1,2].

3. Numerical technique

The numerical predictions described in this paper were performed using the Lagrangian approach provided by the

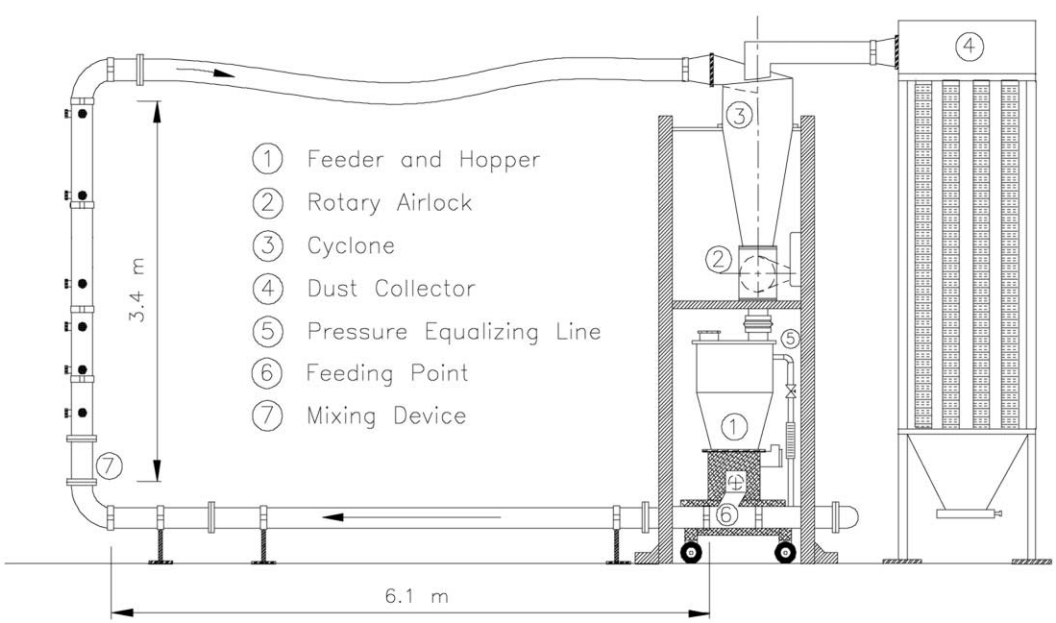

Fig. 2. Experimental test facility.

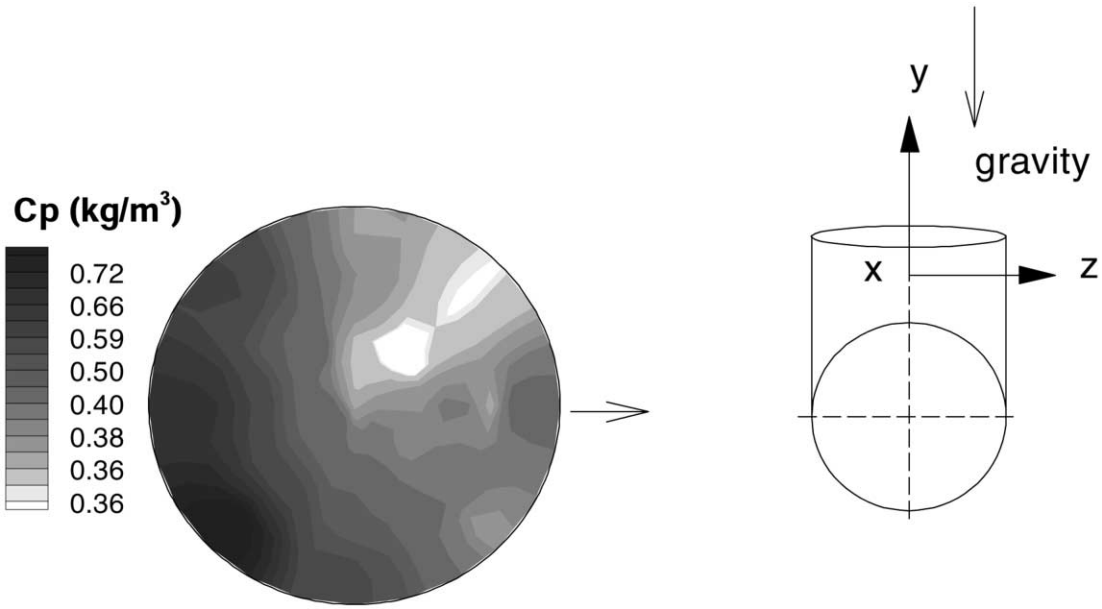

Fig. 3. Measured inlet particle concentration distribution one diameter upstream of the elbow ($A/F = 3.0$; $R_c/D = 1.5$; $U_o = 30$ m/s and $A/F = 3.0$).

CFX-4.2 software package developed by AEA technology [3]. The numerical calculations for the gas phase were performed by solving a set of time averaged Navier–Stokes equations together with the well-known k–ϵ turbulence model of Launder and Spalding [4]. The particles are introduced at a finite number of starting locations. In every given time step, their positions and velocities are calculated according to the forces acting on the particle and using Newton's second law. The equation of motion for a particle can be written as

$$m_p \frac{dV_p}{dt} = F_T \tag{1}$$

where F_T is the total force and includes the drag force (F_D), gravitational force (F_G), and the added mass force (F_A).

$$F_T = F_D + F_G + F_A \tag{2}$$

The major component of the force is the drag force exerted on the particle by the gas phase. This has the form

$$F_D = \frac{1}{8}\pi d^2 \rho C_D |V_R| V_R \tag{3}$$

where the drag coefficient C_D is based on the motion of a single particle and is given by

$$C_D = \frac{24}{Re_p}\left(1 + 0.15\, Re_p^{0.687}\right) \tag{4}$$

$$Re_p = \frac{\rho d_p |V_R|}{\mu} \tag{5}$$

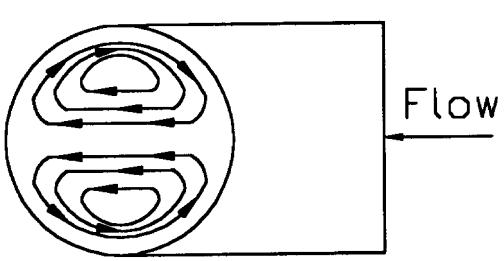

Fig. 4. Secondary flow pattern at the exit of an elbow.

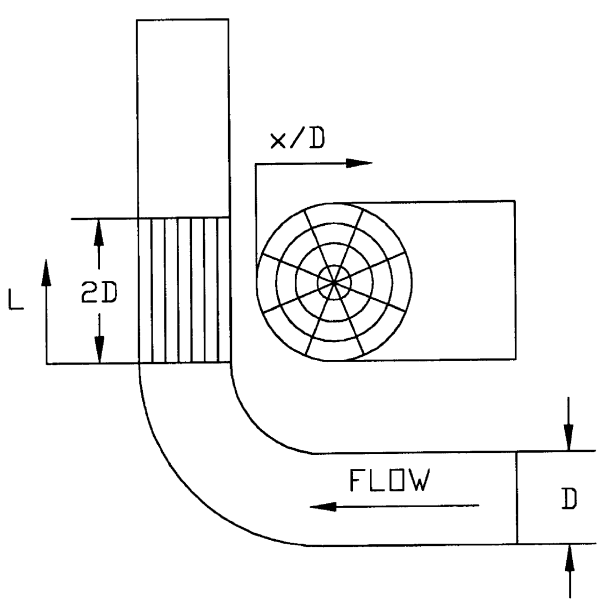

Fig. 5. Flow straightener geometry.

The gravitational force is given by

$$F_G = \frac{1}{6}\pi d^3(\rho_p - \rho)g \quad (6)$$

and the added mass force (virtual force) is given by

$$F_A = -\frac{1}{12}\pi d^3 \rho \frac{dV_p}{dt} \quad (7)$$

The gas phase velocity in the momentum equations is taken to be the mean velocity plus a contribution due to the turbulence, which is assumed to be made up of a collection of randomly directed eddies. The interactions between these eddies and the particles are taken into account by a stochastic procedure, referred to as the eddy life time concept. Particle interactions with the wall are computed using a coefficient of restitution coefficient equal to 0.9.

3.1. Boundary conditions

At the inlet to the horizontal section (downstream of (6) in Fig. 2), a fully developed turbulent velocity profile was specified for the air,

$$U_g = U_{center}\left(1 - \frac{r}{R}\right)^{1/7} \quad (8)$$

At the exit of the vertical test section, the total mass flow rate of gas out of the flow domain was set equal to that specified at the inlet. Since this exit boundary condi-

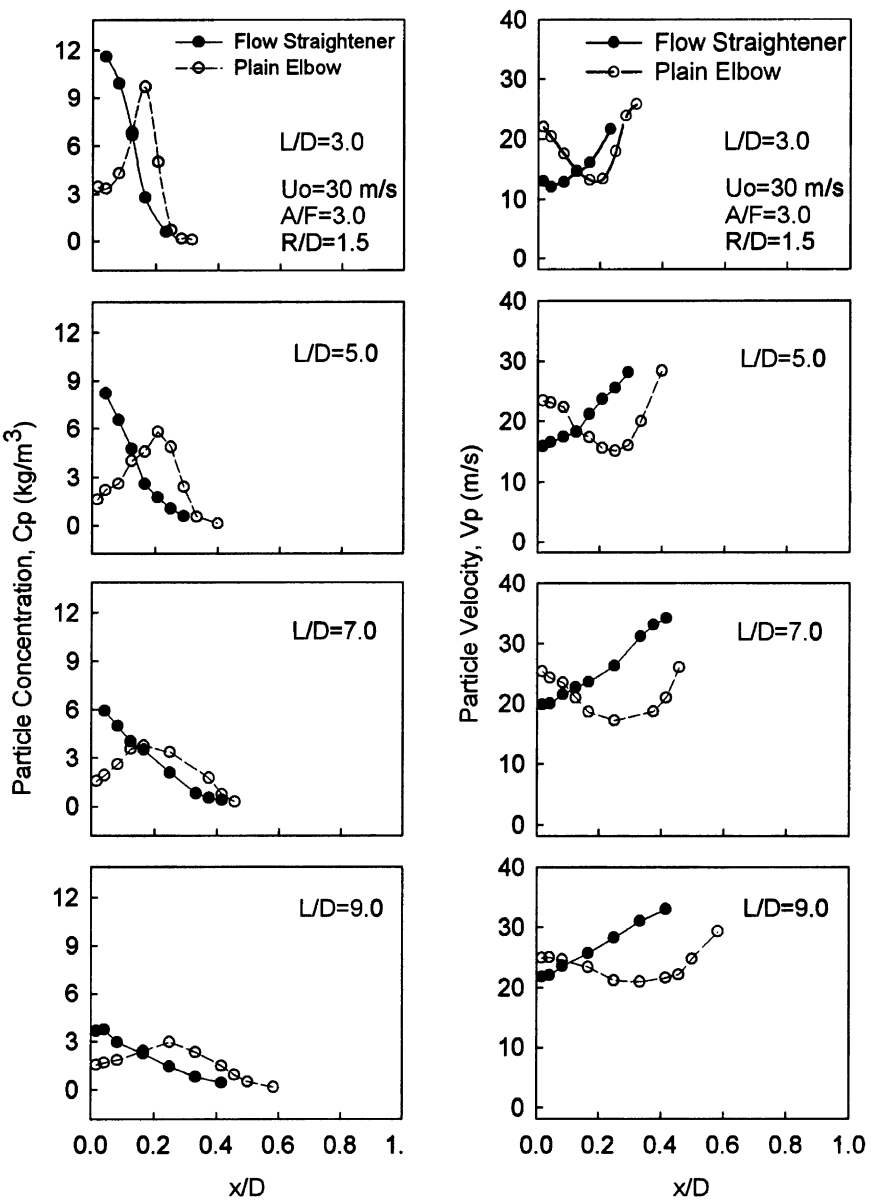

Fig. 6. Comparison of particle concentration profiles for $A/F = 3.0$ (plain elbow, $R_c/D = 1.5$ and flow straightener).

tion was specified downstream far from the elbow, a fully developed flow was assumed at this location; and the axial gradients of all transported variables were set to zero. No-slip boundary conditions at the wall and the wall function concept were used for the near wall regions of the gas flow, eliminating the necessity of extremely fine grids in these regions.

Measurements showed that the particle distribution in the horizontal section upstream of the elbow was not completely uniform. Therefore, the particle locations, velocities and mass fluxes measured in the horizontal section one diameter upstream of the elbow were used in the numerical calculations as inlet conditions for particles, as shown in Fig. 3.

A total of 5000 computational particles was tracked throughout the flow domain. Each computational particle carried the same flow rate and was assumed to be spherical. The particle diameters were stochastically sampled using a Rossin Rammler distribution function (Eq. (9)) and particle size distribution information obtained from the sieve analysis given in Table 1.

$$\text{Prob}(\text{Diameter} > d) = \exp\left[-\left(\frac{d}{d_{\text{m}}}\right)^{n}\right] \tag{9}$$

The quantity d_{m} is the mean particle diameter and n is the spread of the data from the mean, calculated as 59 μm and 2.64, respectively.

Details of the numerical method and solution algorithm are described in Ref. [5].

4. Rope dispersion mechanisms

Secondary motions in pipe bends arise due to the response of a viscous element to an imbalance between the centripetal acceleration and the cross-stream pressure gradient induced by lateral curvature of the main flow. As a result, the axial velocity profile is distorted and the point at which the velocity has its peak is shifted towards the outer wall. An accentuated double vortex flow structure occurs in the fluid phase (Fig. 4) and a significant phase separation in the particulate phase is experienced within the bend geometry due to the density differences and to the centrifugal forces. Upon exiting from the bend, the particles flow together in a narrow localized stream, which is referred to as a particle rope. The dispersion of a particle rope is achieved mainly by flow turbulence and the accentuated double vortex flow structure created by the elbow.

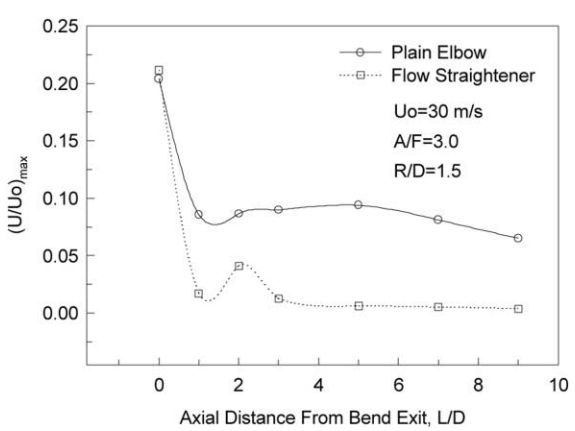

Fig. 7. Normalized maximum transverse velocity as a function of axial distance (U_{o}/U).

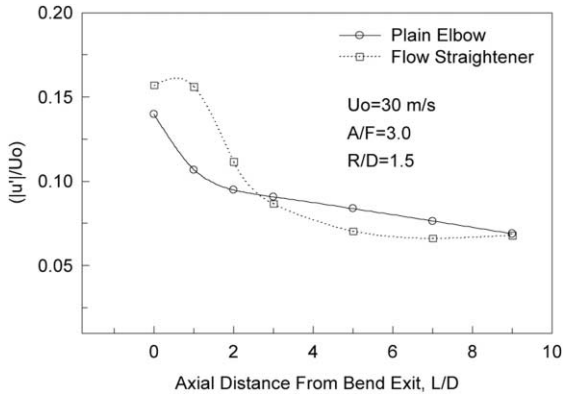

Fig. 8. Turbulent intensity of the air as a function of axial distance ($|u'|/U_{\text{o}}$).

Recently, Yilmaz [1] studied both the rope formation process and the individual effects of secondary flows and flow turbulence on rope dispersion downstream of a plain elbow using the CFX-Flow3D software. The numerical simulation results showed that the secondary velocities transported the particles from within the rope to the particle-free regions while the flow turbulence was responsible for localized mixing in the region immediately adjacent to the rope.

In the present study, the effect of secondary velocities on the rope dispersion characteristics was studied experimentally. In order to eliminate the secondary velocities, a flow straightener was placed at the beginning of the vertical section following the elbow. The flow straightener had eight peripheral and three radial elements in a 0.308-m-long (two pipe diameters) pipe section. The location and the geometry of the flow straightener are shown in Fig. 5.

Fig. 6 shows the radial variations of the particle concentration and velocity distributions downstream of the flow straightener for $A/F = 3.0$ and $U_{\text{o}} = 30$ m/s. The rope structure stayed attached to the outer pipe wall at all elevations, resulting in the largest particle concentrations at the wall. In the vicinity of the outer pipe wall, the acceleration of the particles within the particle rope was significantly reduced, probably due to particle–particle and particle–wall interactions. Moreover, the particles within the rope occupied a small portion of the pipe cross-section even at higher elevations ($L/D = 9.0$), indicating that the

particle transport in the radial direction of the pipe cross-section was negligible in the absence of secondary velocities.

In order to compare the dispersion characteristics between the cases with and without the flow straightener, fiber optic measurements were performed for both cases for the same flow conditions ($R_c/D = 1.5$, $U_o = 30$ m/s, $A/F = 3.0$). The measured particle concentrations and velocities are compared at 3.0, 5.0, 7.0 and 9.0 pipe diameters from the pipe bend exit plane in Fig. 6. As can be seen, the rope dispersion characteristics for each flow configuration occurred differently. The most prominent difference between the two cases is that the peak particle concentrations with the flow straightener are larger than those without the flow straightener (plain elbow) at all elevations. In addition, the rope remained attached to the outer wall in the vertical pipe downstream of the flow straightener, while it moved towards the midsection of the pipe for the case without a flow straightener. This suggests that the secondary flows not only carry the particles around the pipe circumference but also move the rope structure away from the outer wall.

There are also some differences in the particle axial velocity profiles for these two cases. The particle velocity profiles downstream of the bend without a flow straightener (plain elbow) resembled the letter "U", with larger velocities at the edges of the rope and smaller velocities at the center. On the other hand, the particle velocity changed

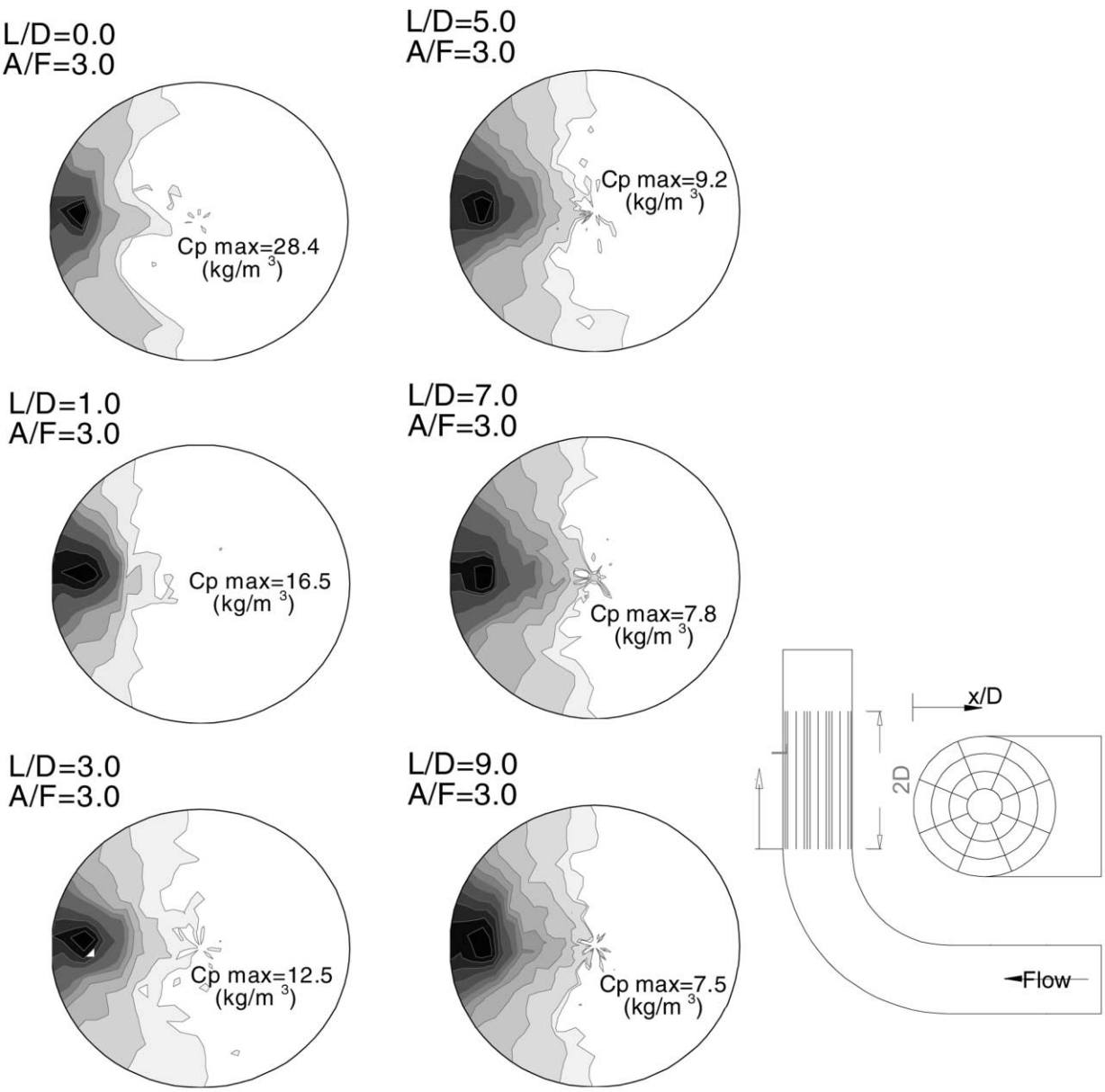

Fig. 9. Predicted particle concentration contours downstream of the flow straightener.

almost linearly with the *x*-axis for the case of a flow straightener, having the minimum values at the wall and the maximum values at the edge of the rope.

Numerical simulations were performed for the cases of the plain elbow and the flow straightener. The primary objectives of the numerical simulations were to investigate the effects of the flow straightener on both the rope structure and the flow field and to understand the mixing processes occurring in each flow configuration.

The CFD simulations for the cases with and without the flow straightener showed that the gas phase secondary velocities after the flow straightener (2D from the elbow exit) were significantly reduced as shown in Fig. 7. On the other hand, the turbulence intensity in the gas phase was only slightly affected by the flow straightener (see Fig. 8).

Fig. 9 shows the contour plots of the predicted particle concentrations in the pipe cross-section at different axial distances away from the bend exit for the case with a flow straightener. It can be seen from these plots that the particles did not spread over the pipe cross-section, as they normally do without a flow straightener. However, a reduction in the predicted maximum particle concentration from 28.4 (at the exit of the bend, $L/D = 0.0$) to 7.5 kg/m^3 (at $L/D = 9.0$) indicated that localized particle mixing occurred inside the region adjacent to the outer wall. Localized particle mixing is probably due to a combination of flow turbulence and particle–wall and particle–particle interactions.

The numerical results were validated by comparing the CFD results with the experimental data obtained with the fiber optic probe. Fig. 10 shows comparisons of predicted particle concentrations with the measured data at four different axial distances away from the bend exit for $A/F = 3.0$ and $U_o = 30$ m/s for the case of the flow

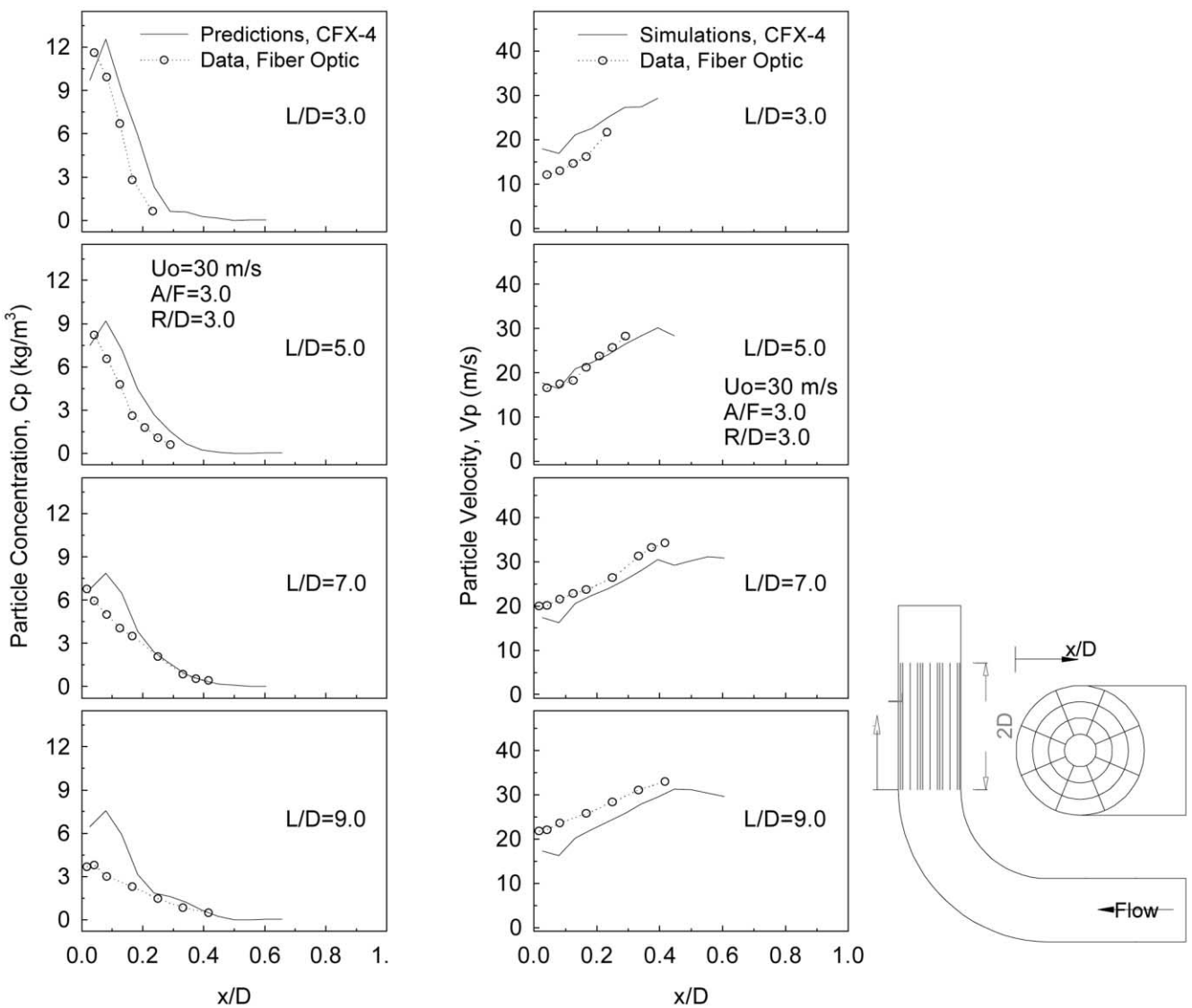

Fig. 10. Comparisons of particle concentrations and velocities downstream of the flow straightener.

conditioner. In general, the predicted results show good agreement with the experimental data, particularly at the elevations close to the elbow exit ($L/D = 3.0$ and 5.0). However, the numerical simulations were not able to predict the measured rapid dispersion rate in particle concentration further downstream of the elbow ($L/D = 7.0$ and 9.0). These differences most likely occurred because the present model does not account for particle–particle and irregular particle–wall interactions.

Comparisons of particle velocities at different axial distances from the bend exit show that the profiles of axial velocity were in good agreement with the numerical simulations (Fig. 10). However, the numerical calculations slightly overestimated the particle velocities at three diameters downstream of the bend, while the particle velocities were underestimated after seven diameters downstream of the elbow. In general, however, the predicted particle concentrations and velocities can be considered in very good agreement with the experimental data when the complexity of the flow is taken into consideration.

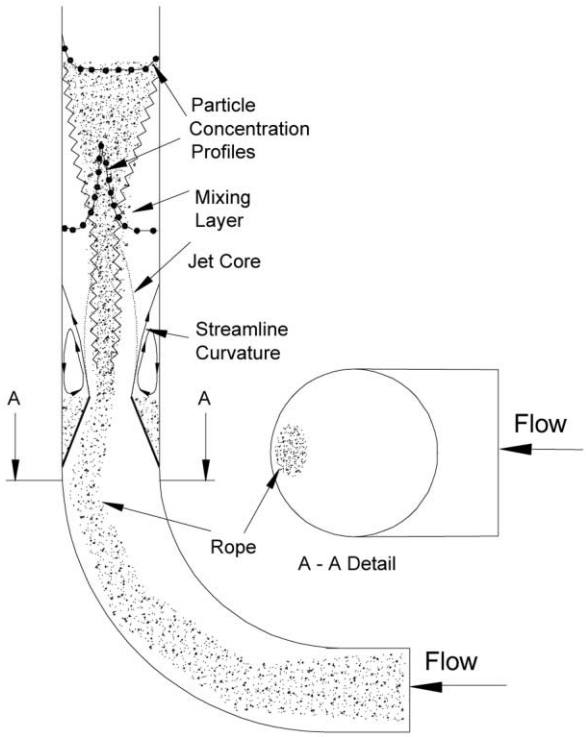

Fig. 12. Sketch of the jet mixing mechanism downstream of a nozzle.

5. Rope dispersion with mixing devices

5.1. Nozzles

The possibility of dispersing a particle rope in a turbulent jet flow formed by a convergent nozzle was investigated. Nozzles having a constant nozzle throat height to diameter ratio (H/D) of 0.8 and beta ratios of 0.5, 0.67 and 0.83 were studied. The nozzle beta ratio (β) is defined as the ratio of the nozzle bore diameter to the pipe diameter. The nozzle geometry and a schematic of the test section are shown in Fig. 11.

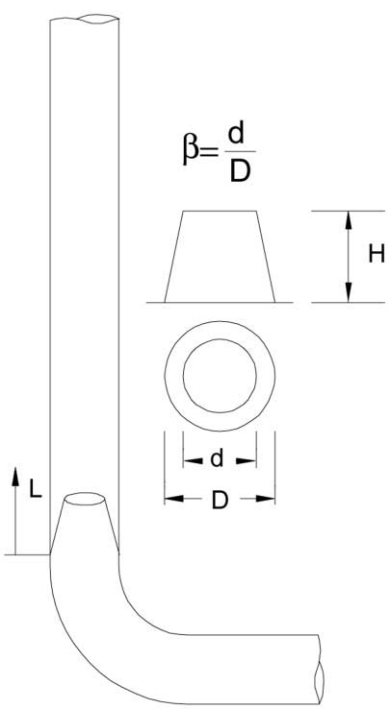

Fig. 11. Nozzle geometry.

Previous jet studies showed that the basic physical mechanism responsible for particle dispersion in jet flows is the mixing layer, where the flow is dominated by a series of large-scale longitudinal vortices [6,7]. These longitudinal vortices result in the presence of streamline curvature downstream of the nozzle exit, which then moves some particles towards the pipe wall. The mixing layer and the region of streamline curvature are sketched in Fig. 12.

Local particle concentrations and velocities were measured using the fiber optic probe at four axial distances from the bend exit plane ($L/D = 3.0$, 5.0, 7.0, and 9.0). These measurements were performed on the pipe symmetry axis by traversing the probe along the x-axis (symmetry axis) from the outer wall to inner wall (from $x/D = 0.0$ to $x/D = 1.0$).

The effect of nozzle β ratio and the air-to-solids loading ratios (A/F) on rope dispersion were studied by comparing time-averaged particle concentration and velocity profiles downstream of the flow. Figs. 13 and 14 show the radial variations of the particle concentration and velocity profiles as functions of β at four different axial distances ($L/D = 3.0$, 5.0, 7.0 and 9.0), for a conveying velocity of 30 m/s, and for air-to-solids loading ratios of $A/F = 3.0$ and 1.0. As can be seen from these figures,

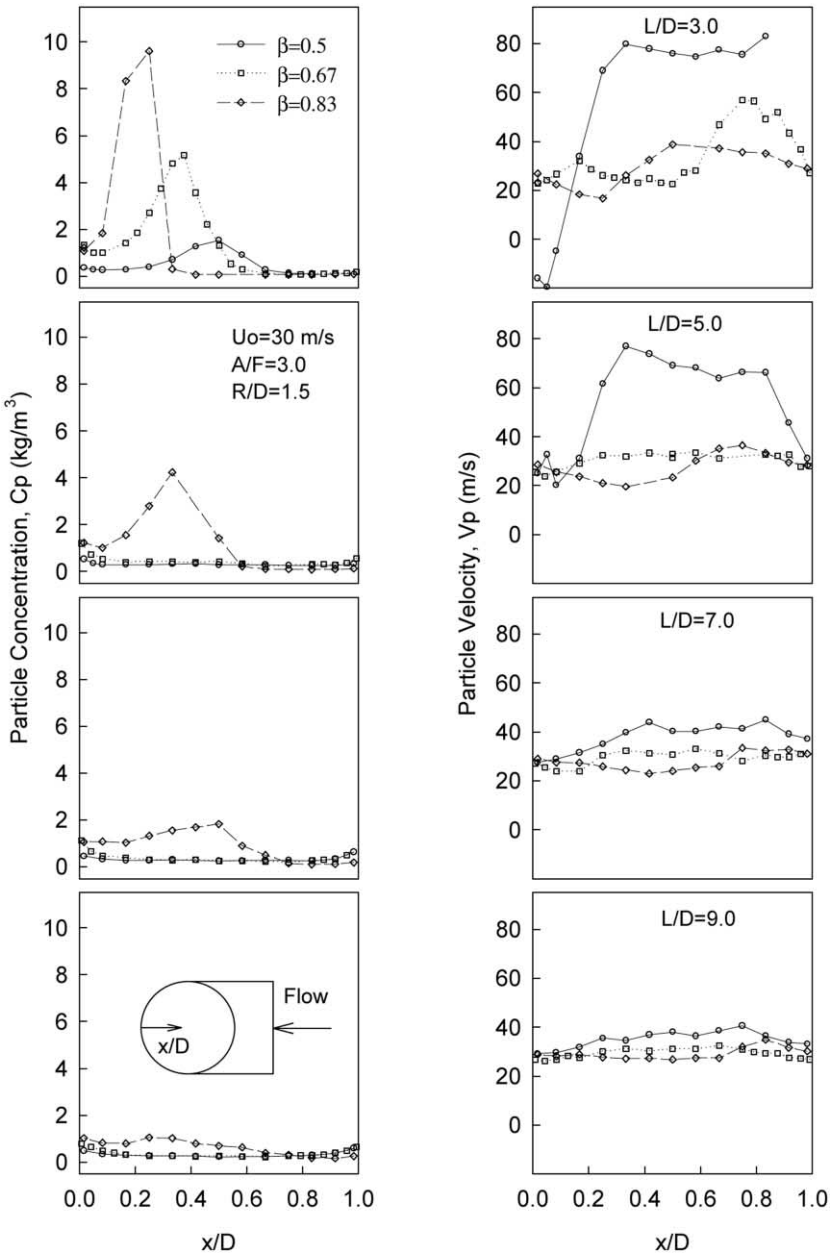

Fig. 13. Measured radial variations of the particle concentration and velocity profiles as a function of nozzle beta ratio (β) ($U_o = 30$ m/s; $A/F = 3.0$; $L/D = 3.0$, 5.0, 7.0 and 9.0).

there are significant non-uniformities in measured particle concentrations and velocities, particularly at three diameters away from the bend exit. At $L/D = 3.0$, the largest particle concentration (or strongest rope-like structure) was measured downstream of the $\beta = 0.83$ nozzle, while the $\beta = 0.5$ nozzle created the lowest peak particle concentration. The dispersion of the rope structure was almost complete five diameters downstream of the bend exit for $\beta = 0.5$ and 0.67. However, a non-uniform particle concentration and velocity distribution persisted until nine diameters downstream of the bend exit for the nozzle with $\beta = 0.83$.

The CFD predictions of the particle concentration and velocity profiles downstream of the nozzles with $\beta = 0.5$ and 0.67 are compared with the measurements performed by the fiber optic probe in Figs. 15 and 16. A total of 5000 spherical particles was tracked through the flow domain. The effect of the flow turbulence on the particle behavior was modeled by a stochastic method proposed by Gosman and Ionnides [16]. However, the influence of the particles on fluid turbulence was not modeled. While the interactions between particles and the wall were modeled using a coefficient of restitution, particle–particle interactions were ignored.

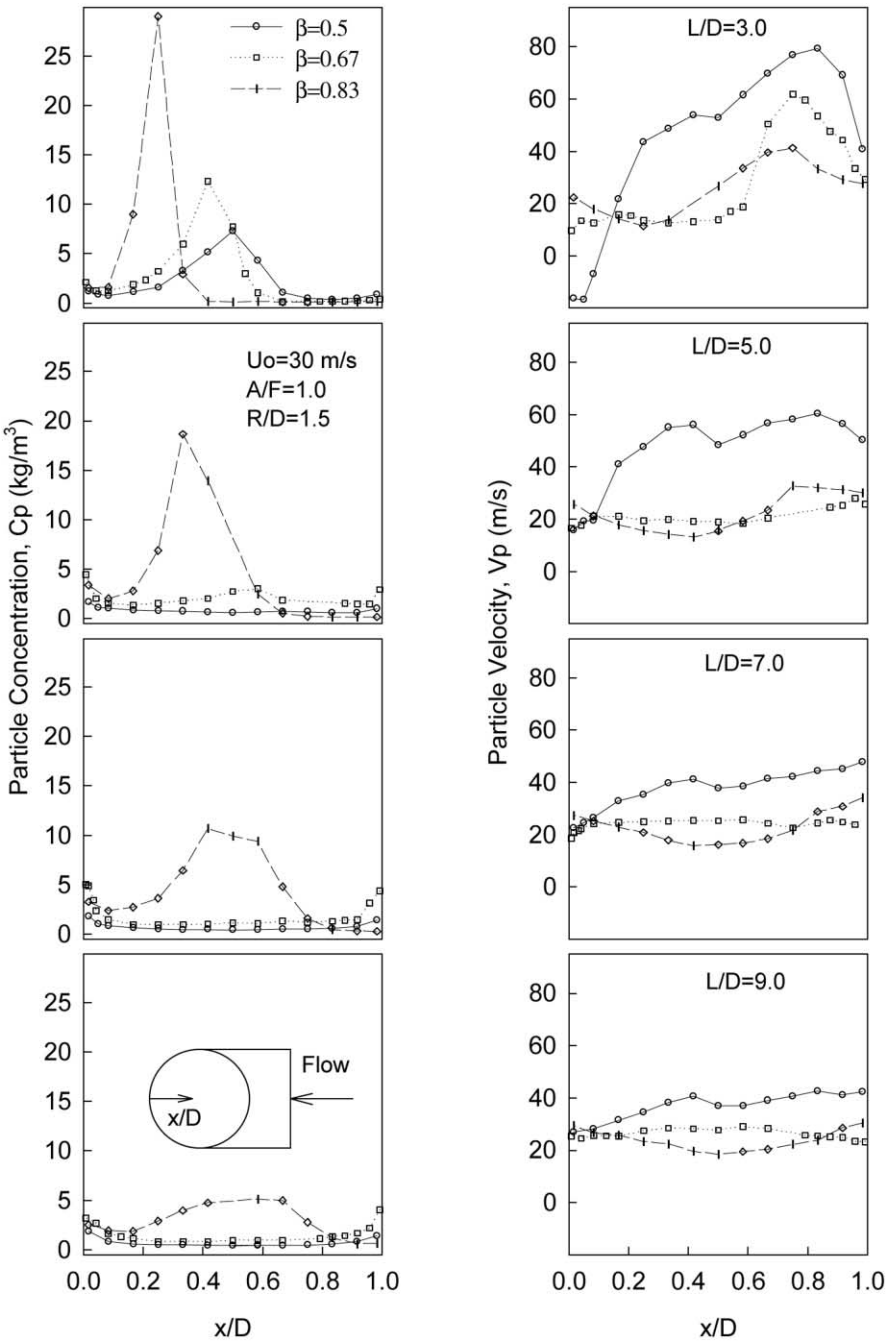

Fig. 14. Measured radial variations of the particle concentration and velocity as a function of nozzle beta ratio (β) ($U_o = 30$ m/s; $A/F = 1.0$; $L/D = 3.0$, 5.0, 7.0 and 9.0).

The magnitude of the peak particle concentration, observed in the center of the pipe at $L/D = 3.0$, was underestimated by the CFD predictions for both nozzle beta ratios. On the other hand, the particle concentrations at the pipe wall were overestimated by the CFD predictions. However, the CFD predictions were able to qualitatively predict the presence of particle restratification in the vicinity of the wall. For $\beta = 0.5$ and 0.67, "U" shaped particle concentration profiles were observed after approximately five diameters downstream of the elbow. The local increase in the mean particle concentration adjacent to the wall was produced by longitudinal vortices (or streamline curvature) which carried the particles into the viscous sublayer where they became trapped [7].

In order to facilitate a quantitative comparison between the cases, a mixing index (MI) was defined based on the

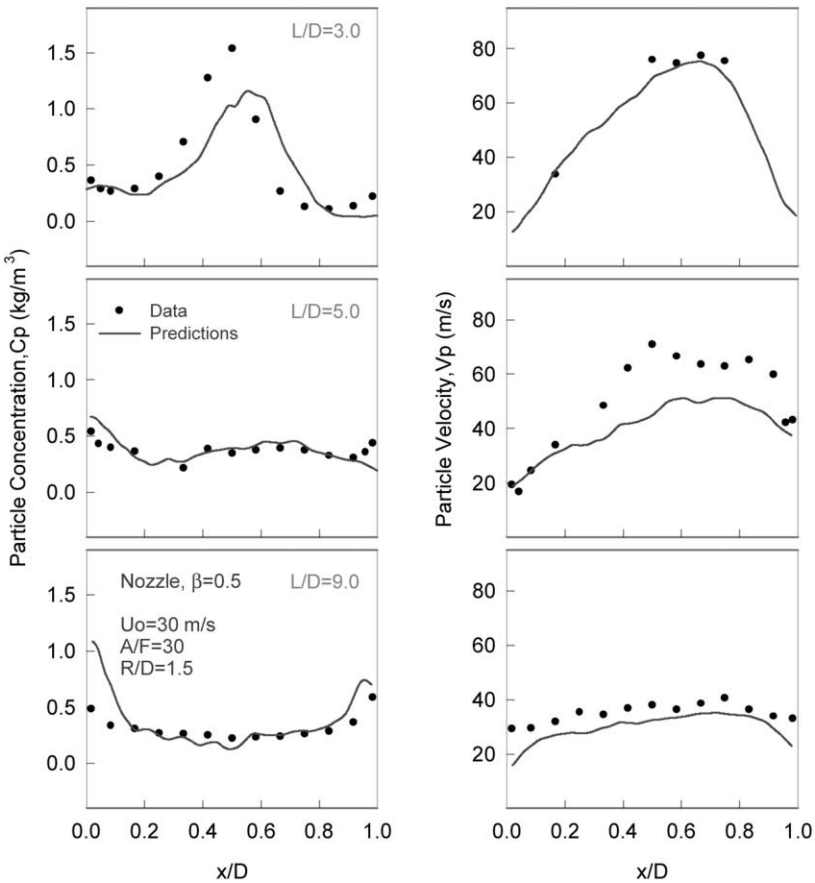

Fig. 15. Comparisons of particle concentration and velocity distributions downstream of a nozzle with $\beta = 0.5$.

particle concentration profile along the pipe diameter at a given axial location. The mixing index (MI) was computed using:

$$\mathrm{MI} = \frac{1}{C_\mathrm{p}}\left[\frac{1}{n-1}\sum_{k=1}^{n}\left(C_\mathrm{m}(k) - C_\mathrm{p}\right)^2\right]^{1/2} \qquad (10)$$

where C_p is the mean particle concentration in the pipe cross-section, $C_\mathrm{m}(k)$ is the local particle concentration measured at equally spaced radial locations in the x-direction, and n is the total number of measurements along the pipe diameter. Eq. (10) gives the degree of variation in concentration as a standard deviation. The flow is assumed to be well mixed when MI tends to zero. The mixing performance for each flow condition was estimated and compared by using the mixing index parameter.

Fig. 17 shows MI for four combinations of U_o and solids loading with the $\beta = 0.5$ nozzle. The restratification phenomenon described in earlier paragraphs is particularly noticeable from these curves at larger values of L/D with $U_\mathrm{o} = 15$ m/s. Fig. 18 compares the values of MI for the three nozzles, all with $U_\mathrm{o} = 30$ m/s and $A/F = 3.0$. These results show there were large improvements in mixing as the nozzle β ratio was reduced from 0.83 to 0.5.

5.2. Lateral jet injection

The use of air jets to break up a particle rope and avoid saltation in long horizontal pipes was first suggested by Weintraub, in a discussion of Patterson's paper [8]. However, no study has been reported since then to investigate the effect of air jets on rope dispersion. In a study by Johnson and Means [9], air jets were used in an attempt to reduce erosion in bends. In the Johnson and Means' study, the erosion rate in a 90° elbow with an air injection was reduced by about 50% compared to that for a standard 90° elbow.

In the present study, the use of air jets was investigated as a possible rope dispersion technique. A jet injector was designed to create an air jet in a plane perpendicular to the main flow stream as shown in Fig. 19. In preliminary experiments, the effect of jet flow rate on the mixing performance was studied by varying the injected flow rate. These measurements were performed at seven pipe diameters away from the bend exit for three different jet flow rates (m_i). These results show fairly well dispersed flow structures at the measurement location with an air injection rate of 5.4% of the total flow rate in the pipe (see Fig. 20).

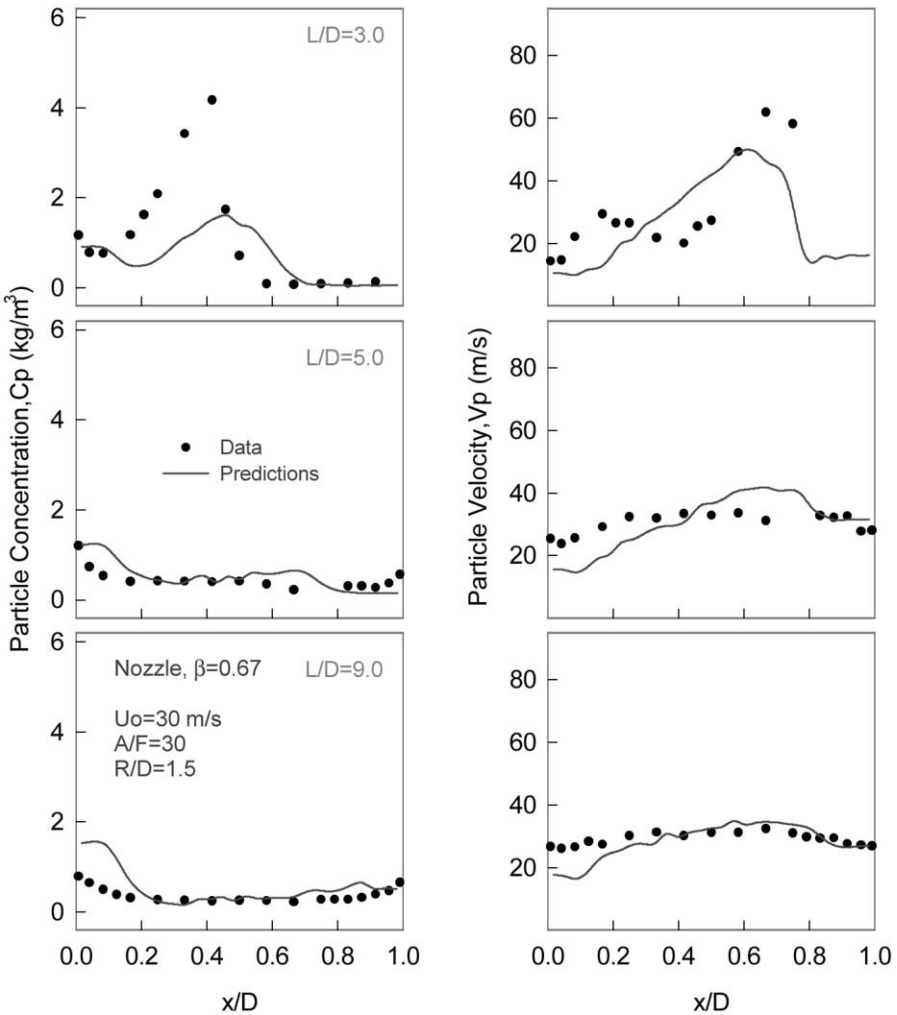

Fig. 16. Comparisons of particle concentration and velocity distributions downstream of a nozzle with $\beta = 0.67$.

In order to determine the best orientation for the jet injector, three different circumferential positions were then tested. The mixing performance with each configuration was first evaluated by visual inspection using a transparent

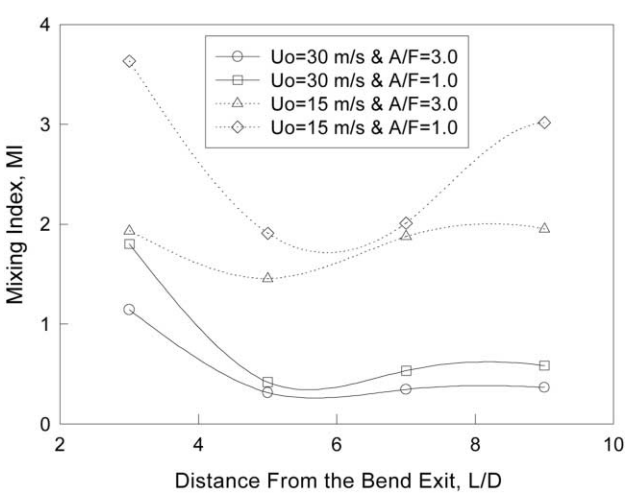

Fig. 17. Mixing indices for the $\beta = 0.5$ nozzle.

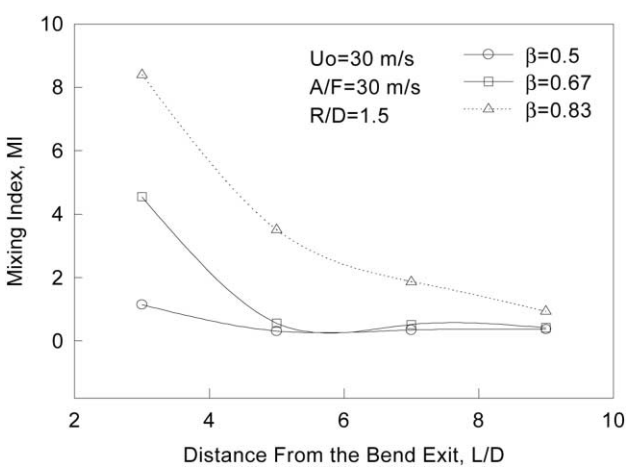

Fig. 18. Mixing indices for nozzles with $\beta = 0.5$, 0.67 and 0.83 ($U_o = 30$ m/s; $A/F = 3.0$; and $R_c/D = 1.5$).

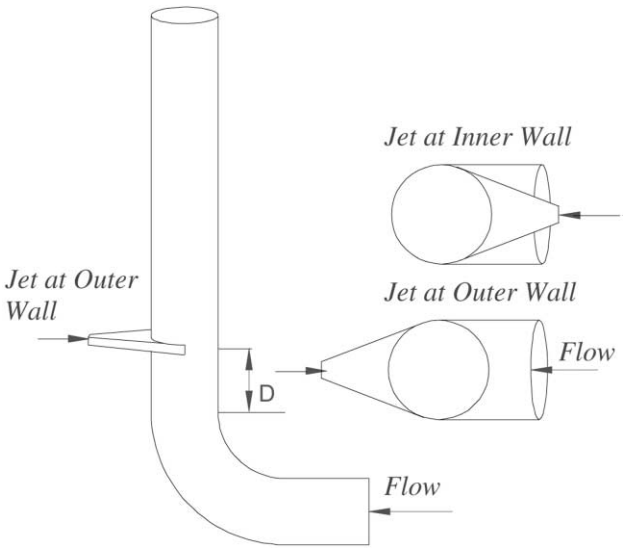

Fig. 19. Plane jet injection system for inner and outer jets.

test section, which was located between $L/D = 2.0$ and 4.0. Detailed fiber optic measurements were then performed. According to the visual observations, the jet injector was able to destroy the rope better when it was located either at the inner wall (inner jet) or outer wall (outer jet) (see Fig. 19). The least effective rope dispersion was observed when the jet injector was located on a side wall.

Detailed fiber optic measurements were performed for two jet configurations, inner jet and outer jet, for a constant normalized jet flow rate (m_i) of 5.4% and for a conveying air velocity of 30 m/s. In addition, the effect of air-to-solids loading ratio was investigated for each configuration. Since the flow was not symmetrical about the *x*-axis, the fiber optic measurements were performed over the pipe cross-section by traversing the probe along the radius at eight circumferential locations, 45° apart from each other. In each case, the jet injector was located one diameter downstream of the bend exit ($L/D = 1.0$) as shown in Fig. 19.

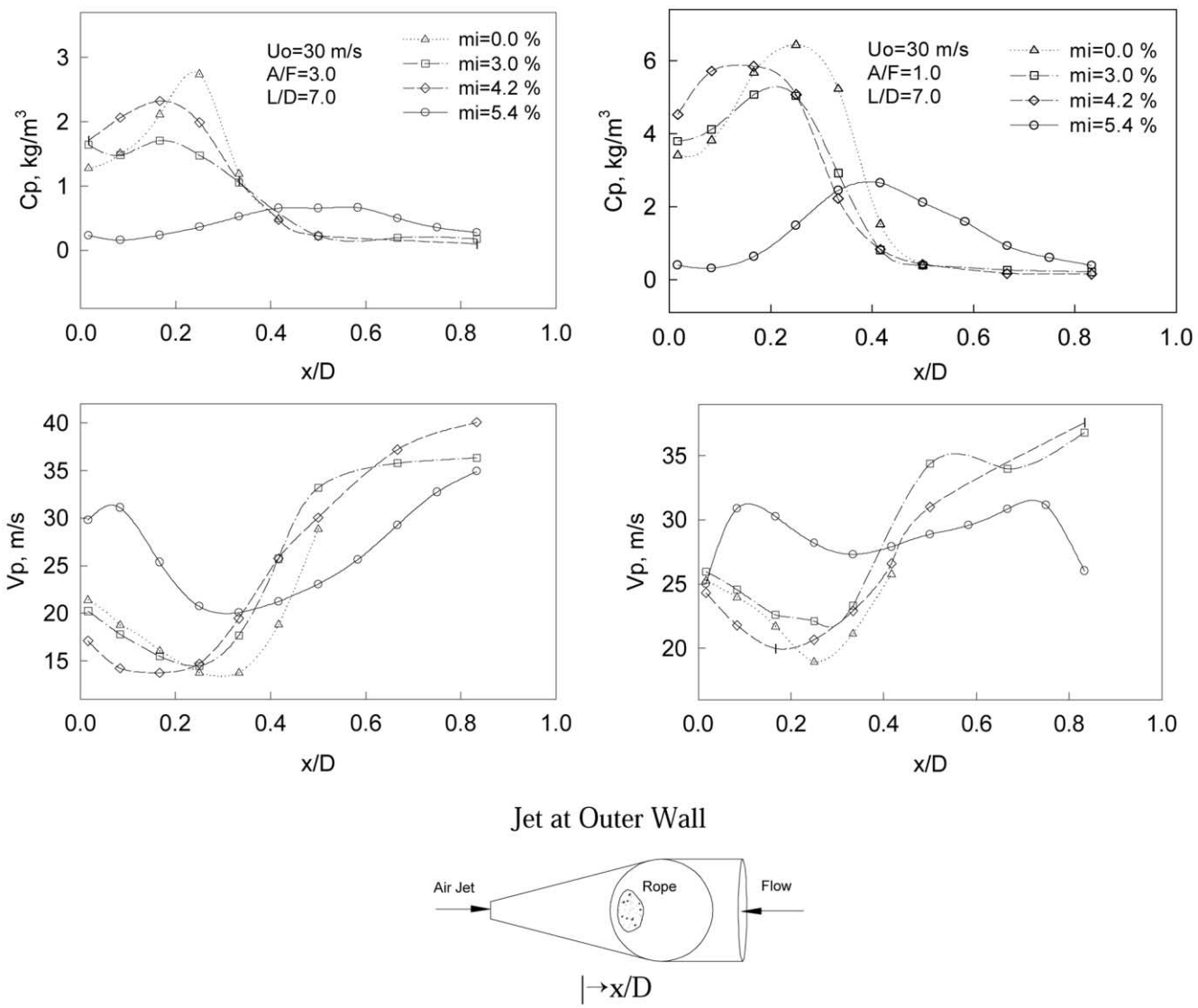

Fig. 20. Effect of air injection rate for $A/F = 1.0$ and 3.0.

5.2.1. Plane jet from inner wall

Fig. 21 illustrates the particle concentration contour plots for $A/F = 3.0$ and 1.0. At three diameters away from the bend exit plane, the particle rope was positioned unsymmetrically, having moved towards a side wall. The asymmetrical particle concentration distribution at $L/D = 3.0$ was probably caused by nonuniformities in the particle concentration distribution in the horizontal pipe upstream of the elbow.

However, at five and seven diameters downstream of the bend exit, the particle concentrations, were fairly symmetrically distributed over the pipe cross-section. The majority of the particles were located in the central region with peak particle concentrations (C_p) ranging from 1.0 to 2.0 (kg/m^3). These C_p values are significantly lower than those for the case of the plain elbow (no flow mixing device).

5.2.2. Plane jet from outer wall

The experiments were repeated for the case when the jet injector was positioned at the outer wall (referred to as outer jet). The particle concentration contour plots at dif-

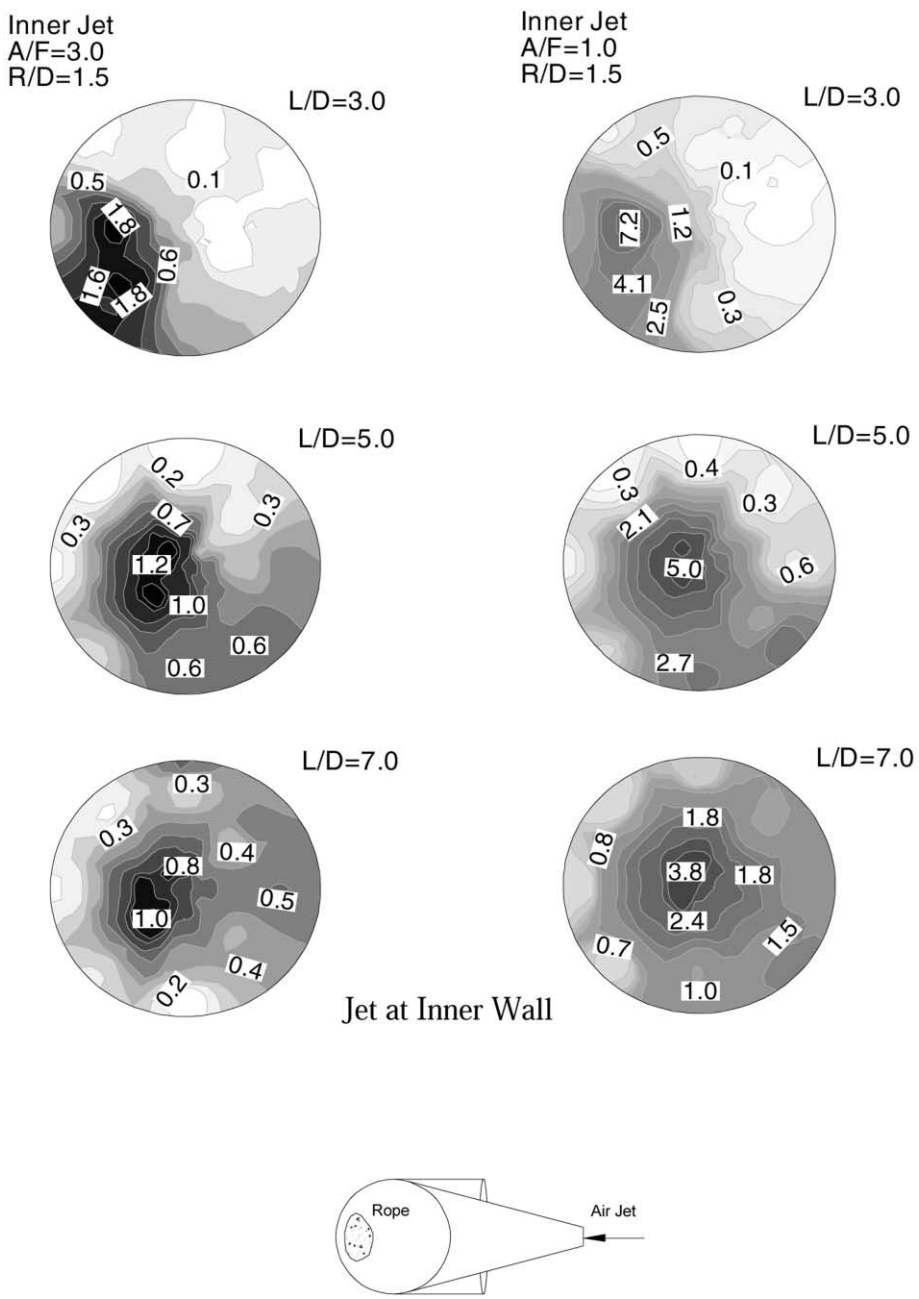

Fig. 21. Measured particle concentration contours downstream of the inner jet injector for $A/F = 3.0$ and $U_o = 30$ m/s.

ferent axial distances are shown in Fig. 22. The particle rope does not appear to be affected by the air jet at three diameters away from the bend exit plane for either solids loading rate ($A/F = 3.0$ and 1.0), however, the effect of the air jet is clearly seen at $L/D = 5.0$. At this location ($L/D = 5.0$ for $A/F = 3.0$ and 1.0), the rope was divided into several small ropes, each of which had relatively low particle concentrations and was located at a side wall. Moreover, downstream of the mixing plane, the flow exhibited a rotational particle motion. Once again, this probably occurred because of the asymmetrical particle distribution in the horizontal inlet pipe. The rotational motion was more pronounced for low solids loading rate ($A/F = 3.0$).

Quantitative comparisons between the inner and outer jets were made by using the mixing index (Fig. 23). These comparisons reveal that the inner jet established a more homogeneous flow distribution over the pipe cross-section. These results clearly show how the orientation of the jet injector is important to obtaining optimal mixing.

5.3. Swirl vanes

Swirling two-phase flows are encountered in many engineering applications, including combustion systems and cyclone separators. Extensive research efforts have been expended in understanding and characterizing the effects of swirling flows [10–13].

The degree of swirl usually is characterized by a swirl number S, which is a nondimensional number representing the axial flux of angular momentum divided by the product of the pipe radius and axial momentum flux. The swirl number is defined as follows,

$$S = \frac{\int_0^R uvr^2 \mathrm{d}r}{R\int_0^R v^2 r \mathrm{d}r} \tag{11}$$

where u and v are tangential and axial velocities, respectively, and R is the pipe radius.

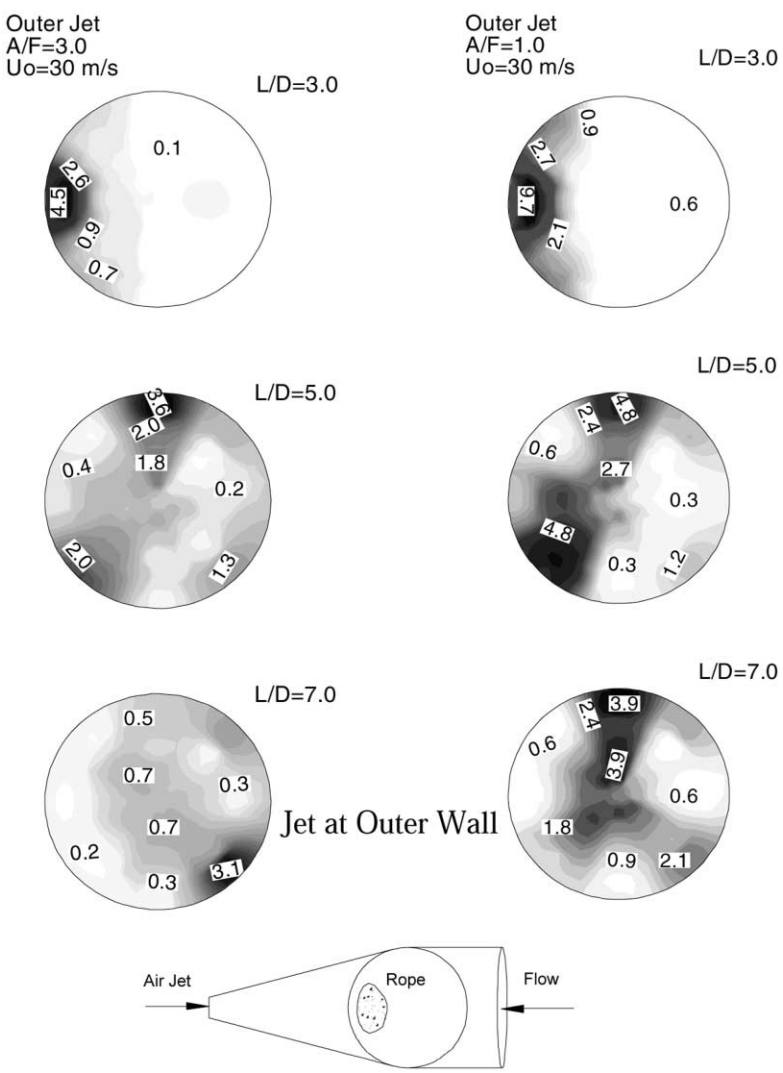

Fig. 22. Measured particle concentration contours downstream of the outer jet injector for $A/F = 1.0$ and 3.0 and $U_o = 30$ m/s.

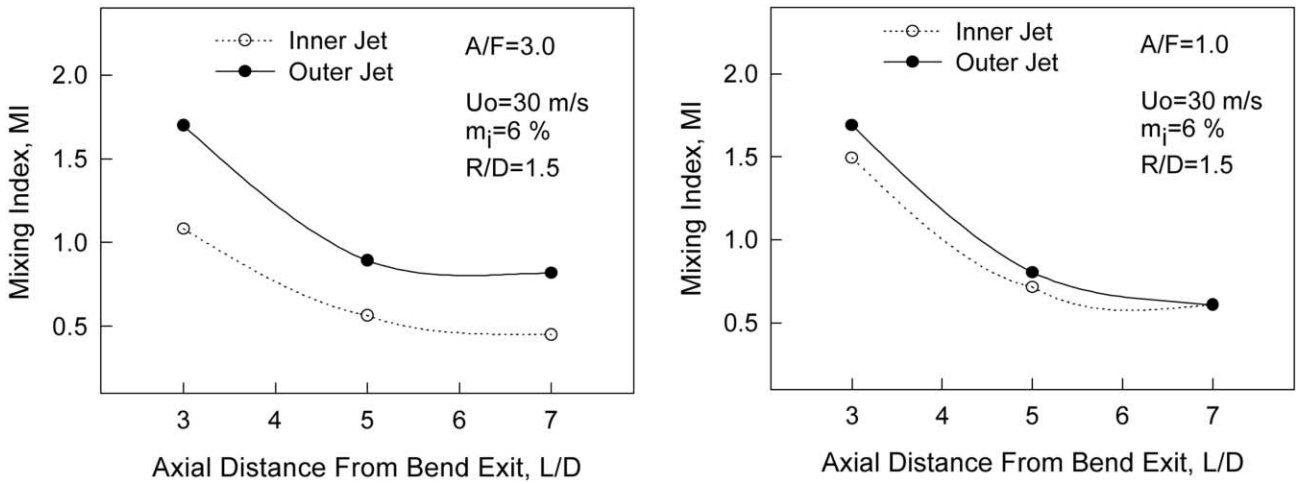

Fig. 23. Comparison of mixing indices between inner jet and outer jet for $A/F = 3.0$ and 1.0.

Recently, swirling flow has been applied to pneumatic conveying systems to reduce pressure drop, pipe blockage, pipe wear, and particle deposition [14].

In the present study, the swirling flow was used to disperse the particle rope created by the elbow. The calculation of the swirl number (S) was based on the swirl vane angle, ϕ, as suggested by Lilley [10].

$$S \approx \frac{2}{3}\tan\phi \qquad (12)$$

For vane angles of 15, 30 and 60, for example, approximate swirl numbers are 0.2, 0.4 and 1.2, respectively. Here 100% efficiency is assumed for the swirl vanes.

Fig. 24 shows a sketch of the experimental test section, where a counter-clockwise rotation was generated at the exit of the elbow, between $L/D = 0.0$ and 2.0, using vaned swirlers. Two different designs for generating swirling motion were used. In the first design, eight swirl vanes were installed inside the test section, providing a swirl number (S) of 0.13. In the second design, a swirl number (S) of 0.26 was achieved with four swirl vanes placed inside the test section. Therefore, the results show the combined effects of both the swirl number and the number of swirl vanes on the rope dispersion characteristics.

The fiber optic probe measurements of particle concentration were performed over the pipe cross-section at three different axial locations for $A/F = 3.0$ and $U_o = 30$ m/s. Fig. 25 illustrates the particle concentration and velocity contours for $S = 0.13$ and 0.26. It can be seen from Fig. 25 that for the $S = 0.13$ case, the rope created by the elbow was split into several rope-like structures by the swirl vanes and each individual flow structure spiraled around the pipe circumference. These smaller rope structures had relatively small particle concentrations compared to the original rope (here, the term "original rope" refers to the rope exiting the 90° elbow). Although the original rope was destroyed by the swirl vanes, the rotational motion of each smaller particle rope persisted further downstream. More importantly, the peak particle concentration of each rotating particle structure remained relatively unchanged as the flow moved downstream. In fact, a slight increase in the peak particle concentration was observed after three pipe diameters from the bend exit. As mentioned by Hirai and Takagi [15], owing to the body force field resulting from the swirling motion, a counter effect of the swirling motion was observed further downstream of the flow, and the particle mixing was retarded.

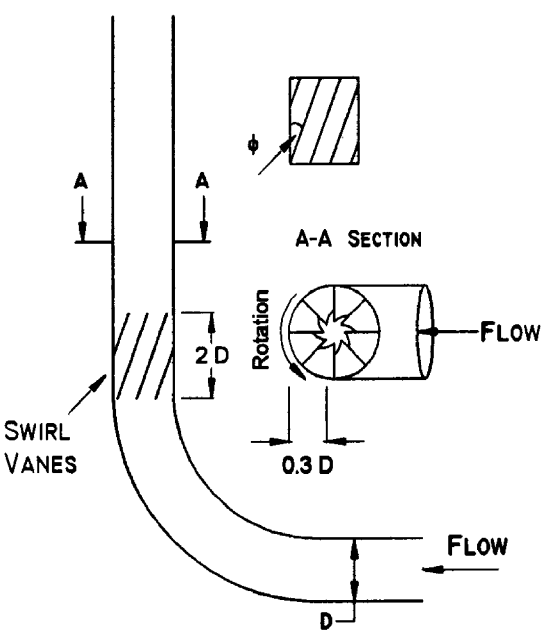

Fig. 24. Experimental test section and swirl vanes.

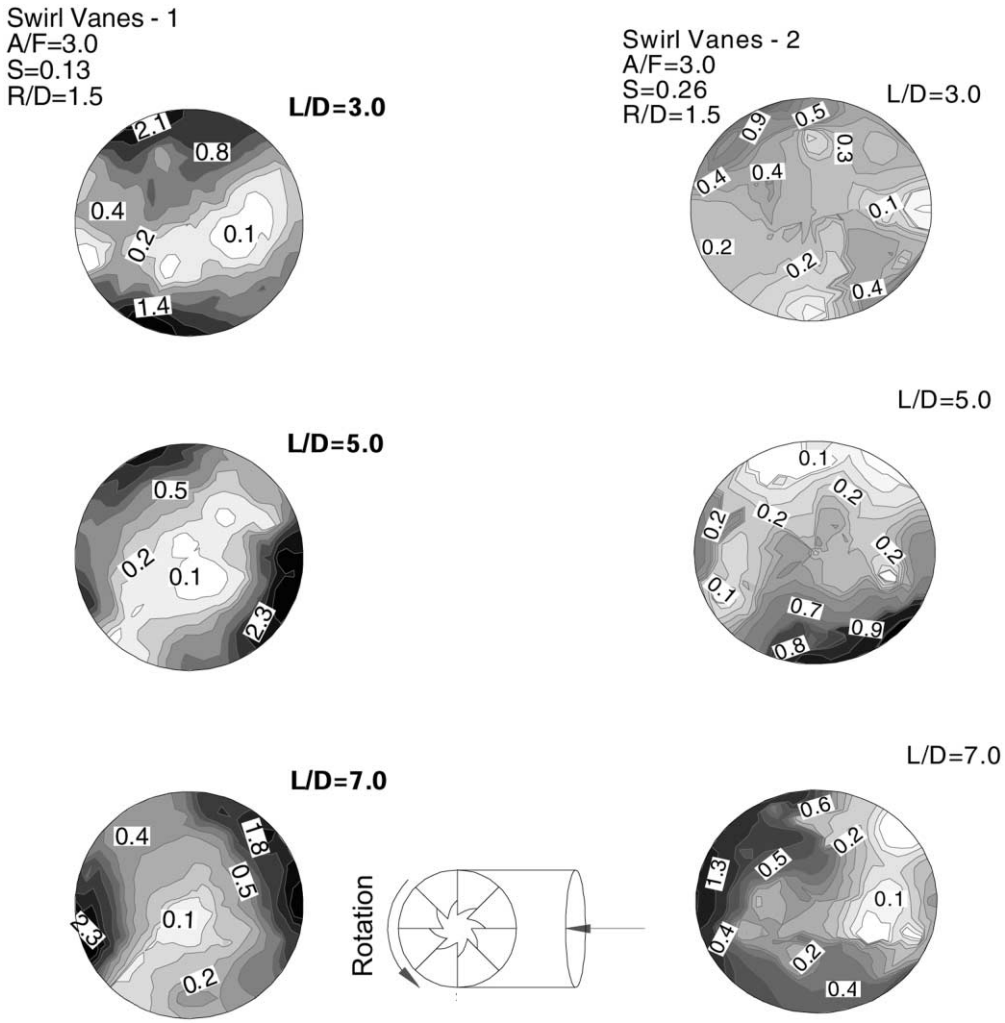

Fig. 25. Particle velocity and concentration contours for $S = 0.13$ ($A/F = 3.0$, $U_o = 30$ m/s and $R_c/D = 1.5$).

The mixing index values for both swirl numbers are compared in Fig. 26. As can be seen from this figure, the values of the mixing indices slightly increased further downstream of the swirl vanes, indicating a strengthening of the smaller rope structures.

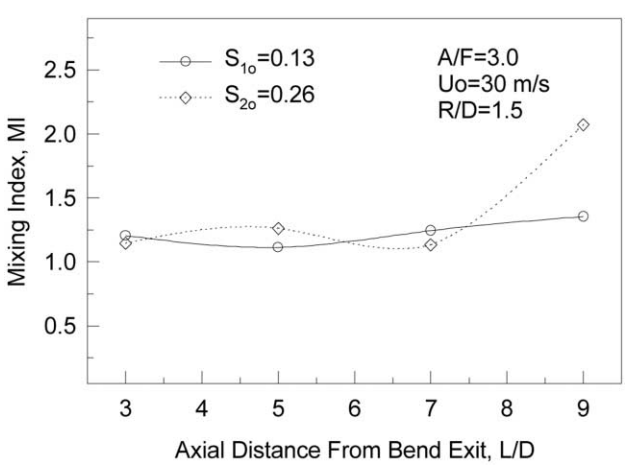

Fig. 26. Mixing index values as a function of axial distance.

6. Summary and conclusions

Rope dispersion characteristics in the absence of secondary flows were investigated in the first part of this study. It was observed that the rope dispersion rate was significantly reduced when the double vortex structure formed by the elbow was eliminated with a flow straightener installed immediately after the elbow. Furthermore, no significant particle dispersion in the radial direction towards the inner wall was observed in the absence of the flow straightener. These findings confirm the importance of secondary velocities in transporting the particles from within the rope to the particle-free regions.

In the second part of the study, the rope dispersion characteristics of several types of mixing devices were studied. These included convergent nozzles, air jet injection, and swirl vanes.

The fiber optic measurements for the $\beta = 0.5$ and 0.67 nozzles showed that the local particle concentration at the pipe wall increased slightly after approximately three diameters downstream of the bend exit, caused by a partial restratification of the flow further downstream. Moreover, a strong dependency of rope dispersion on the conveying air velocity, air-to-solids loading ratios, and nozzle beta ratios was found, with more uniform particle distribution over the pipe cross-section occurring for higher conveying air velocities, lower solids loadings and smaller beta ratios.

All mixing techniques, except the $\beta = 0.83$ nozzle, were able to disperse the particle rope within nine pipe diameters from the bend exit plane. However, there are some disadvantages of these designs for practical applications. For instance, the nozzles with $\beta = 0.5$ and 0.67 cause excessive pressure drop. The pressure drop caused by the $\beta = 0.83$ nozzle was 9 kPa (36 in. H_2O) for an average conveying air velocity of 30 m/s and $A/F = 3.0$. The air jet injection technique requires additional fan power and also increases the total flow rate of conveying fluid carried by the pipe. With swirl vanes, an effect of swirling motion on particle mixing was observed further downstream of the flow. As a consequence of the centrifugal forces, local particle concentration increased at the pipe wall, causing some particle restratification as the particles were transported downstream.

The CFD predictions are in good agreement with the measurements performed with the fiber optic probe. Despite slight differences from the experimental data, the CFD predictions were able to predict the most important flow phenomena observed by the measurements.

Nomenclature

A	Pipe cross-section area (m^2)
A/F	Air-to-fuel mass flow rate ratio (–)
C_D	Drag coefficient (–)
C_p	Particle mass concentration ($C_p = \rho_p(1-\epsilon)$), (kg/m^3)
C_μ	k–ϵ model constant
D	Inside pipe diameter (m)
d	Orifice or nozzle bore diameter (m)
d_p	Particle diameter (μm)
d_m	Mean particle diameter (μm)
e	Coefficient of restitution
F_D	Drag force (N)
F_T	Total force acting on a particle (N)
L/D	Axial dimensionless distance downstream of the elbow exit (m)
m_I	Normalized injected jet flow rate
$\dot{m}_p$	Solids mass flow rate (kg/s)
R_c	Radius of curvature of elbow (m)
Re_p	Particle Reynolds number ($Re_p = \rho\lvert\vec{U}_R\rvert d_p/\mu$)
S	Swirl number
St	Stokes number ($St = \rho_p d_p U_o/18\mu D_T$)
U	Local fluid velocity (m/s)
U_o	Conveying air velocity (m/s)
u', v', w'	Fluctuating air velocities (m/s)
$\lvert u'\rvert$	rms air velocity $\left(\lvert u'\rvert = \sqrt{\overline{u'^2}} = \sqrt{\frac{2}{3}k}\right)$, (m/s)
V_p	Particle velocity (m/s)
V_R	Relative particle velocity (with respect to air) ($U_a - V_p$)
v'_p	rms particle velocity $\left(\lvert u'_p\rvert = \sqrt{\overline{u'^2_p}}\right)$, (m/s)
x/D	Dimensionless transverse distance from outer wall of elbow (m)
x, y	Transverse distances in pipe cross-section (m)

Greek letters

ρ_p	Particle density (kg/m^3)
μ	Fluid viscosity (kg/ms)
ρ	Air density (kg/m^3)
ϕ	General Variable
β	Ratio of orifice diameter to pipe diameter ($\beta = d/D$)
ϵ	Turbulence dissipation rate (m^2/s^3) and Voidage ($\epsilon = 1 - V_p/V_T$)

References

[1] A. Yilmaz, Roping Phenomena in Lean Phase Pneumatic Conveying, Lehigh University, PhD Dissertation, 1997.

[2] A. Yilmaz, E.K. Levy, Particle Velocity and Concentration Measurements in Lean Phase Pneumatic Conveying Using a Fiber Optic Probe, Proceedings of 1998 ASME Fluids Engineering Division Meeting, Fluid Measurement and Instrumentation Forum, Paper No. FEDSM98-5282, Washington, DC, 1998-b.

[3] CFX-4.2 User Manual. Computational Fluid Dynamics Services, AEA Technology, Harwell, England, 1997.

[4] B.E. Launder, D.B. Spalding, The numerical computation of turbulent flows, Comp. Meth. Appl. Mech. Eng. 3 (1974) 269–289.

[5] H. Bilirgen, Mixing and Dispersion of Particle Ropes in Lean Phase Pneumatic Conveying, Lehigh University, PhD Dissertation, 2000.

[6] C.T. Crowe, M. Sommerfeld, Y. Tsuji, Multiphase Flows with Droplets and Particles, CRC Press, 1998.

[7] J.K. Eaton, J.R. Fessler, Preferential concentration of particles by turbulence, Int. J. Multiphase Flow 20 (1994) 169–209.

[8] R.C. Patterson, Pulverized coal transport through pipes, J. Eng. Power (1959) 43–54.

[9] E.K. Johnson, K.H. Means, Erosion studies in pneumatic transport bends, Engineering Foundation Conference—Pneumatic and Hydraulic Conveying Systems, April 21–25, 1996.

[10] D.G. Lilley, Review: swirl flows in combustion, AIAA J. 15 (1977) 1063–1078.

[11] M. Sommerfeld, H.H. Qiu, Characterization of particle-laden, confined swirling flows by phase-doppler anemometry and numerical calculations, Int. J. Multiphase Flow 19 (19) (1993) 1093–1127.

[12] H. Li, Y. Tomita, Experimental study of swirling flow pneumatic conveying system in a vertical pipeline, J. Fluids Eng., Trans. ASME 120 (1) (1998) 200–203.
[13] H. Li, Y. Tomita, Experimental study of swirling flow pneumatic conveying system in a horizontal pipeline, J. Fluids Eng., Trans. ASME 118 (3) (1996) 526–530.
[14] H. Li, Y. Tomita, K. Funatsu, Research of swirling flow pneumatic conveying system in a horizontal pipeline, Trans. ASME 58 (1992) 1599–1604.
[15] S. Hirai, T. Takagi, Parameters dominating swirl effects on turbulent transport derived from stress–scalar–flux transport equation, Int. J. Heat Mass Transfer 38 (12) (1995) 2175–2182.
[16] A. Gosman, E. Ionnides, Aspects of computer simulation of liquid-fueled combustors, AIAA paper. No. 81-0323 (1981).